












Amorphous carbon thin films: Mechanisms of hydrogen incorporation during magnetron sputtering and consequences for the secondary electron emission

C. F. Adame ; E. Alves ; N. P. Barradas ; P. Costa Pinto ; Y. Delaup; I. M. M. Ferreira ; H. Neupert ; M. Himmerlich ; S. Pfeiffer ; M. Rimoldi ; M. Taborelli ; O. M. N. D. Teodoro; N. Bundaleski 



J. Vac. Sci. Technol. A 41, 043412 (2023)

<https://doi.org/10.1116/6.0002759>



View
Online



Export
Citation

CrossMark



HIDEN ANALYTICAL Instruments for Advanced Science

- Knowledge
- Experience
- Expertise

Click to view our product catalogue

Contact Hiden Analytical for further details:
www.HidenAnalytical.com
info@hiden.co.uk

| Gas Analysis | Surface Science | Plasma Diagnostics | Vacuum Analysis |
|---|---|---|---|
| <ul style="list-style-type: none">dynamic measurement of reaction gas streamscatalysis and thermal analysismolecular beam studiesdissolved species probesfermentation, environmental and ecological studies | <ul style="list-style-type: none">UHV-TPDSIMSend point detection in ion beam etchelemental imaging - surface mapping | <ul style="list-style-type: none">plasma source characterizationetch and deposition process reaction kinetic studiesanalysis of neutral and radical species | <ul style="list-style-type: none">partial pressure measurement and control of process gasesreactive sputter process controlvacuum diagnosticsvacuum coating process monitoring |

Amorphous carbon thin films: Mechanisms of hydrogen incorporation during magnetron sputtering and consequences for the secondary electron emission

Cite as: J. Vac. Sci. Technol. A 41, 043412 (2023); doi: 10.1116/6.0002759

Submitted: 12 April 2023 · Accepted: 1 June 2023 ·

Published Online: 23 June 2023



View Online



Export Citation



CrossMark

C. F. Adame,¹ E. Alves,^{2,3} N. P. Barradas,^{2,3} P. Costa Pinto,⁴ Y. Delaup,⁴ I. M. M. Ferreira,⁵ H. Neupert,⁴ M. Himmerlich,⁴ S. Pfeiffer,⁴ M. Rimoldi,⁴ M. Taborelli,⁴ O. M. N. D. Teodoro,¹ and N. Bundaleski^{1,a)}

AFFILIATIONS

¹Department of Physics, CEFITEC, Nova School of Science and Technology 2829-516 Caparica, Portugal

²DECN, Instituto Superior Técnico, University of Lisbon, 2695-066 Bobadela, Portugal

³IPFN, Instituto Superior Técnico, University of Lisbon, 1049-001 Lisbon, Portugal

⁴European Organization for Nuclear Research, CERN, 1211 Geneva 23, Switzerland

⁵Materials Science Department, i3N/CENIMAT, Nova School of Science and Technology, 2829-516 Caparica, Portugal

^{a)}Electronic mail: n.bundaleski@fct.unl.pt

ABSTRACT

Amorphous carbon (a-C) films, having low secondary electron yield (SEY), are used at CERN to suppress electron multipacting in the beam pipes of particle accelerators. It was already demonstrated that hydrogen impurities increase the SEY of a-C films. In this work, a systematic characterization of a set of a-C coatings, deliberately contaminated by deuterium during the magnetron sputtering deposition, by scanning electron microscopy, ion beam analysis, secondary ion mass spectrometry, and optical absorption spectroscopy was performed to establish a correlation between the hydrogen content and the secondary electron emission properties. In parallel, the mechanisms of contamination were also investigated. Adding deuterium allows resolving the contributions of intentional and natural contamination. The results enabled us to quantify the relative deuterium/hydrogen (D/H) amounts and relate them with the maximum SEY (SEY_{max}). The first step of incorporation appears to be formation of D/H atoms in the discharge. An increase in both the flux of deposited carbon atoms and the discharge current with a D_2 fraction in the gas discharge can be explained by target poisoning with deuterium species followed by etching of C_xD_y clusters, mainly by physical sputtering. For overall relative D/H amounts between 11% and 47% in the discharge gas, the SEY_{max} increases almost linearly from 0.99 to 1.38. An abrupt growth of SEY_{max} from 1.38 to 2.12 takes place in the narrow range of D/H relative content of 47%–54%, for which the nature of the deposited films changes to a polymer-like layer.

© 2023 Author(s). All article content, except where otherwise noted, is licensed under a Creative Commons Attribution (CC BY) license (<http://creativecommons.org/licenses/by/4.0/>). <https://doi.org/10.1116/6.0002759>

I. INTRODUCTION

Electrons, resonantly accelerated in an RF field toward the chamber walls of a vacuum system, can be multiplied in an avalanche process sustained by secondary electron emission. This event, known as electron multipacting, can limit the performance of high-power RF devices of utmost importance in space applications but also of high-intensity particle accelerators.^{1–5} In the latter case, electron clouds formed in this way can cause

beam instabilities, pressure increase, and heat load in the cryogenic parts of a system.^{6–8}

One way to efficiently suppress electron multipacting is to keep the secondary electron yield (SEY) of the chamber walls, defined as the average number of electrons emitted per incident electron, below a certain threshold. In the case of particle accelerators, this threshold depends on the aperture of the beampipe, on any applied electrical or magnetic fields, as well as on bunch

27 September 2023 15:45:06

population and spacing. For the High Luminosity Large Hadron Collider (HL-LHC) at CERN, the threshold lies in the range from 1.1 to 1.3.⁷ Since materials used to produce vacuum chambers (e.g., stainless steel, copper, and aluminum) and RF devices (e.g., Cu) provide technical air-exposed surfaces with a maximum secondary electron yield (SEY_{max}) usually above 1.8, thin films of chemically inert materials with low secondary electron emission are an alternative to reduce SEY_{max} below the threshold for electron multipacting.

Carbon coatings are well established for the reduction of SEY and have proven efficiency for reducing electron multipacting in particle accelerators.⁹ However, the SEY of these films is affected by impurities such as N and H, which can be included during the deposition process. In a previous work,¹⁰ H₂ was deliberately added to the discharge gas (Ar) in fractions up to 0.5%, resulting in an increase of SEY_{max} from 0.98 to 1.38, correlated with an increase of the Tauc gap. The same work reports that the addition of 1% of N₂ to the discharge gas reduces the SEY_{max} , accompanied by a decrease of the Tauc gap, demonstrating also that nitrogen addition can partially mitigate the negative effect of H₂ in the residual gas. Since H can originate from different precursors outgassed from the chamber walls (mainly H₂O, H₂, and hydrocarbons), residual gas pressure and composition are among the main parameters affecting coating quality. In some cases of nonbakeable long beampipes, with low vacuum conductance, hydrogen contamination resulted in films with SEY_{max} above the multipacting threshold value. A typical example is the coating of 12 m long beam pipes with apertures of a few centimeters in diameter being equipped with cryo-adsorbers with extremely high specific surfaces ($\sim 10^4$)¹¹ and yielding high outgassing rates during the deposition process, which resulted in a SEY_{max} above 1.6.¹²

In a well-established qualitative picture of secondary electron emission, SEY should increase when opening an energy gap in the electronic density of states of a material.¹³ The presence of the gap reduces the possible energy loss channels for electrons traveling at energies above the vacuum level and increases the escape depth. As a result, more excited secondary electrons can be emitted and the SEY is higher.

According to this simplified view, opening (closing) of the Tauc gap due to H (N) incorporation into the film increases (decreases) the SEY. Nevertheless, there are still several open questions. First, in Ref. 10, there was no quantitative assessment of the amount of H in thin films so that the concentration causing a particular SEY increase in carbon coatings is not known. It is also not clear how hydrogen is incorporated, how it is bonded in the carbon layer, and how exactly the electronic structure is modified by H incorporation into the material. Answers to these questions are expected to provide guidelines to optimize the coating technology and process.

In this work, we investigate the mechanisms leading to the incorporation of H in amorphous carbon (a-C) coatings deposited by sputtering and its influence on the SEY. For this purpose, a set of coatings was deposited in a magnetron discharge in Ar gas to which different amounts of D₂ were added. The usage of deuterium is motivated by the possibility to distinguish between unavoidable process-related H contamination (i.e., due to outgassing from components in the coating system) and the controlled addition of

impurities to study their influence. Consumption of the injected D₂ was monitored during the process by residual gas analysis and the samples were characterized using various techniques: scanning electron microscopy with a focused ion beam (FIB-SEM) to study the surface morphology and measure the thin film thickness; ion beam analysis (IBA) techniques, namely, elastic recoil detection analysis (ERDA), Rutherford backscattering (RBS), and nuclear reaction analysis (NRA), were used together with secondary ion mass spectrometry (SIMS) for composition analysis, SEY measurements, and optical absorption spectroscopy (OAS) in order to determine the Tauc gaps. This choice of techniques provided a multiperspective view on the characteristics of the coatings, thus revealing details of the deposition process and the mechanism of H incorporation. The latter can then be related to the secondary electron emission properties of the a-C films. Improved understanding of D incorporation into the films provides guidelines for the optimization of the deposition process aiming to reduce H contamination.

II. MATERIALS AND METHODS

Samples were prepared by sputtering from high-purity graphite targets (grade 2020PT from MERSEN, ashes content <20 ppm), using a 50 mm diameter planar magnetron source, and Ar as the discharge gas. Si wafers [boron doped, resistivity 200 Ω cm, orientation (111) from Sil'tronix] and quartz plates (grade Suprasil 300 from WISAG) were used as substrates. Before mounting in the coating system, the substrates were degreased in an ethanol bath with ultrasonic agitation. The distance between the target and the samples was 93 mm. A total of five coating runs were performed with different percentages of D₂ in the Ar discharge gas. The corresponding samples are reference (without D₂ addition), 0.2D (0.2), 0.5D (0.5), 1D (1.3), and 10D (10.9), for which the number in brackets corresponds to the percentages of D₂ in the discharge. Before each coating run, the system was evacuated (by a tandem of a turbomolecular and a scroll pump) and baked for 24h at 230 °C, with the magnetron source kept at ~ 150 °C. This procedure enabled to reach the estimated base pressure in the deposition chamber in the low 10^{-7} Pa range (N₂ equivalent, read by an SVT AL310 AN hot cathode gauge) after cooldown and to minimize the contribution of the residual gas to thin film contamination. The gas composition was monitored by a Residual Gas Analyzer (RGA, Pfeiffer QMA125) in a differentially pumped system with a background pressure below 10^{-8} Pa. Before each run, the RGA was calibrated for deuterium, using a hot cathode gauge (that was previously calibrated against a spinning rotor gauge) as a reference. D₂ is first injected in the deposition chamber, up to the partial pressure required to attain the required fraction, followed by the injection of Ar to fulfill a total pressure of 2 Pa. A new graphite target is used for each coating run and a burn-in procedure is performed for about 120 min with the samples in the parking position (protected from the flux of C atoms), until all parameters have stabilized.

Two batches of grounded substrates were assembled per run. The first one consisted of five Si substrates for SEY ($\times 2$), SIMS ($\times 1$), SEM ($\times 1$) measurements, and a spare substrate. The second batch had two Si substrates for IBA and photoelectron spectroscopy measurements (the latter not included in this work) and two

27 September 2023 15:45:06

quartz substrates for optical measurements. The discharge power was set to 30 W, corresponding to the areal power density of 4.4 W/cm^2 , the latter being obtained by dividing the power with the area of the plasma race track measured on a used target. The first batch is coated for about 15h in order to obtain a thickness of about 150 nm, followed by the coating of the second batch (about 50h for 500 nm). Deposition times were set based on the outcome from preceding calibration runs without added D_2 . In each case, when switching on the deposition system, a drop of D_2 partial pressure was observed, indicating that part of it was consumed during the process. After coating, the system was left to cooldown to room temperature and then vented to dry air (80% of N_2 and 20% of O_2) before sample extraction. The samples remained exposed to air for $\sim 2\text{--}4$ h before being conditioned in stainless steel vacuum chambers, pumped by a turbomolecular pump, filled with N_2 gas, and transferred to different laboratories where the characterizations were performed.

For the characterization of the surface morphology and determination of the coating thickness, a Zeiss Cross Beam 540 FIB-SEM was employed. FIB milling was conducted using a Ga ion beam at an acceleration voltage of 30 kV at normal incidence. Imaging of the milled cross section with the electron beam was conducted at an accelerating voltage of 3 kV and a probe current of 500 pA using an InLens secondary electron detector. The relative uncertainty of the film thickness was estimated to be about 5%.

IBA (ERDA, RBS, and NRA) measurements were performed on a 2.5 MV Van der Graaf accelerator (HVEE, A-type). They consisted of two experiments for each sample, each providing several detected spectra at the same time. A 2 MeV $^4\text{He}^+$ ion beam, impinging the surface at 78° with respect to the surface normal, was used to simultaneously perform ERDA and RBS measurements. ERDA was used to detect the H and D particles recoiled at 24° with respect to the primary beam direction, while the primary ions, backscattered to about 160° in the Cornell geometry (the incident and outgoing angles with respect to the sample surface were 12° and 11.7° , respectively), were detected by the RBS measurements. The latter provided measurements of C and O concentrations. In the second experiment, performed by a 2 MeV $^3\text{He}^+$ beam impinging the surface at normal incidence, ^{12}C and D were detected by NRA, simultaneously with the primary ions backscattered to 155° . Clear observations of the C signal width and the Si edge position enabled the determination of the total film areal density N_t . This quantity represents the total atomic concentration in a film integrated over the film thickness so that N_t/d represents an averaged atomic concentration in the film n , where d is the film thickness. An automated fit was performed in the program NDF (version v10.0b),¹⁴ using a depth profile of the sample composition as fitting parameters to simulate all IBA data and to optimize the fit until the best agreement was found. The electron stopping powers and scattering cross sections were previously calculated with SRIM¹⁵ and SigmaCalc,¹⁶ respectively. Double scattering and pileup were calculated with the algorithms given in Refs. 17 and 18, respectively. The uncertainties of elemental concentrations and the total areal density of the films were determined from a Bayesian inference with a Markov chain Monte Carlo algorithm.^{19,20} A set of 10 000 different simulations, all consistent with the data, was performed for different sets of

parameters. The uncertainties for each parameter are determined as the corresponding standard deviation in the frame of the simulation set. The calculation took into account the counting statistics, the uncertainties of the beam energy, incidence and scattering angle, acceptance solid angle, beam fluence, and energy resolution. It did not consider the uncertainties of the scattering cross sections and the stopping powers. The latter adds systematic uncertainties to the determined quantities (areal densities and concentrations), which are estimated to be around 10% of the contributions of the factors that were considered in the simulations.

SIMS was performed in a nanoTOF II TOF-SIMS (PHI, USA) instrument, using an analysis ion source with Bi_3^+ (30 keV) with 20 ns pulse duration. The sputter etching for depth-profiling was enabled by an Ar^+ (3 keV) ion source that was operated in an interleave mode with a current of 400 nA (sputtering area $400 \times 400 \mu\text{m}^2$), providing a typical sputtering rate of about 0.8 nm/s. Spectra were acquired in the range 0–200 amu, and the base pressure in the analysis chamber was $\sim 5 \times 10^{-7}$ Pa.

For noninsulating samples, the SEY was measured in UHV at a pressure of 5×10^{-8} Pa with an ELG-2 electron gun (Kimball Physics) by the method of alternating sample bias ($V_{SA} = \pm 47.1 \text{ V}$) using an electron current of 3–4 nA focused to a spot diameter of 1 mm. The sample current was measured using an optically isolated amplifier with a gain of 10^8 V/A and a 6517B electrometer (Keithley Instruments). For a negatively/positively biased sample, the primary (I_P)/secondary (I_S) electron current was measured and the SEY was calculated as the ratio I_S/I_P . The estimated dose associated with a single SEY measurement is $\sim 3 \times 10^{-7} \text{ C/mm}^2$.

The samples of type 10D exhibit very low conductivity. Their surface charged up during standard SEY measurements, which perturbs the measurements. Therefore, the SEY was characterized in a pulsed measurement on a second setup, which is represented in Fig. 1.

The whole measurement is performed under UHV conditions at a pressure of 8×10^{-8} Pa. The setup consists of an electron gun

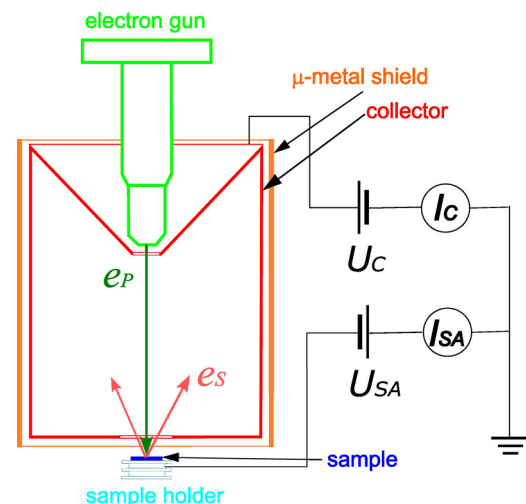


FIG. 1. Schematic representation of the SEY measurement setup for low conductivity samples.

27 September 2023 15:45:06

(ELG-2/EGPS-1022 from Kimball Physics) emitting $5\mu\text{s}$ long pulses of primary electrons e_p impinging on the biased sample (U_{SA} : sample bias, -18 V) at normal incidence. The sample is mounted on a sample holder, just below a collector. The whole setup is shielded by μ -metal to avoid the influence of external magnetic fields. The primary electron energy varies from 40 to 1800 eV from pulse to pulse in discrete steps to cover the whole spectrum. One pulse at a time is used to compute the SEY for the corresponding energy. The primary electron dose per pulse is $1\text{--}2 \times 10^{-12}\text{ C}$. The emitted secondary electrons e_s are collected by the positively biased collector ($U_C = 45\text{ V}$). The corresponding collector current I_C and sample current I_{SA} are measured simultaneously by two current amplifiers (Femto DHPA-100). The total sample current equals the incoming primary beam current I_p subtracted by the outgoing collector current, thus we may write $I_p = I_{SA} + I_C$ when respecting the current flow direction. Signals from the amplifiers are recorded by an oscilloscope (LeCroy waverunner LT354) and numerically integrated to calculate the total charge of collected electrons per pulse on the collector (Q_C) and on the sample (Q_{SA}). SEY was computed as $Q_C/(Q_C + Q_{SA})$.

Optical absorption spectroscopy (OAS) of samples deposited on quartz substrates was performed by means of a UV-VIS-NIR spectrophotometer from JASCO (model V-770). For that purpose, the reflectance $R_{exp}(\lambda)$ and transmittance $T_{exp}(\lambda)$ of each sample were measured in the wavelength range of $\lambda = 200\text{--}2500\text{ nm}$. The absorption coefficient $\alpha(\lambda)$ was used to estimate the energy of the optical band gap for each film from Tauc plots²¹ and was obtained from the extinction coefficient $\kappa(\lambda)$ of the thin film via $\alpha(\lambda) = 4\pi\kappa(\lambda)/\lambda$. The latter was computed by solving for each wavelength, a system of two transcendental equations $R_{exp}(\lambda) = R_{theor}(\lambda, n, \kappa, d)$ and $T_{exp}(\lambda) = T_{theor}(\lambda, n, \kappa, d)$, where R_{theor} and T_{theor} are analytical expressions for the reflectance and transmittance of a bulk material covered with a uniform flat thin film of thickness d , real refractive index $n(\lambda)$, and extinction coefficient $\kappa(\lambda)$.⁵⁰ The system of equations was solved using the 2D Muller algorithm proposed in Ref. 22.

III. RESULTS

A. Surface morphology of the films and the deposition rate

All coatings produced have a smooth surface, as illustrated by the SEM micrographs of the samples deposited on silicon [Fig. 2(a)]. This fact is important in our study since surface morphology can have a significant impact on secondary electron emission.²³ Consequently, one can be assured that SEY differences between samples are exclusively related to their electronic structure. Thickness measurements performed using FIB-SEM enabled us to determine the thickness deposition rate vs the discharge gas composition [Fig. 2(b)], evidencing a monotonic increase with the amount of D_2 in the discharge. Since the relative amount of D_2 is presented in a logarithmic scale, for clarity, the points for the reference sample (containing 0% of deuterium) are placed at 0.01% for all graphs which show the deuterium content in the discharge gas in the logarithmic scale.

Discharge current and voltage are also plotted in Fig. 2(b). The increase in the deposition rate for a higher D content in the discharge gas will be discussed in relation to the film composition analysis in Sec. III B.

B. Composition and density of thin films

The different spectra obtained in the frame of IBA analysis are both highly complementary and corroborating, as explained in Sec. II. The information carried by each spectrum contributes to the final result. The data were analyzed by fitting all spectra simultaneously, in a self-consistent manner, with the depth profile of each element and the total areal concentrations as fitting parameters. As an example of the fitting process, we show in Fig. 3, the data and fits for the sample 0.2D. The accuracy of the obtained composition depends on several experimental (the energy calibration, the charge-solid angle product, and the detector properties in each experiment)

27 September 2023 15:45:06

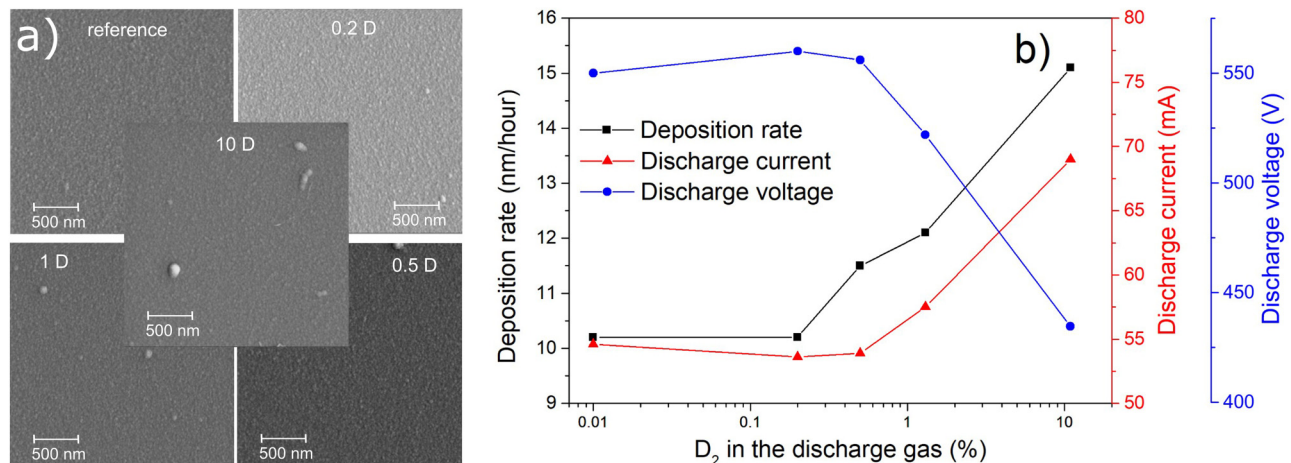
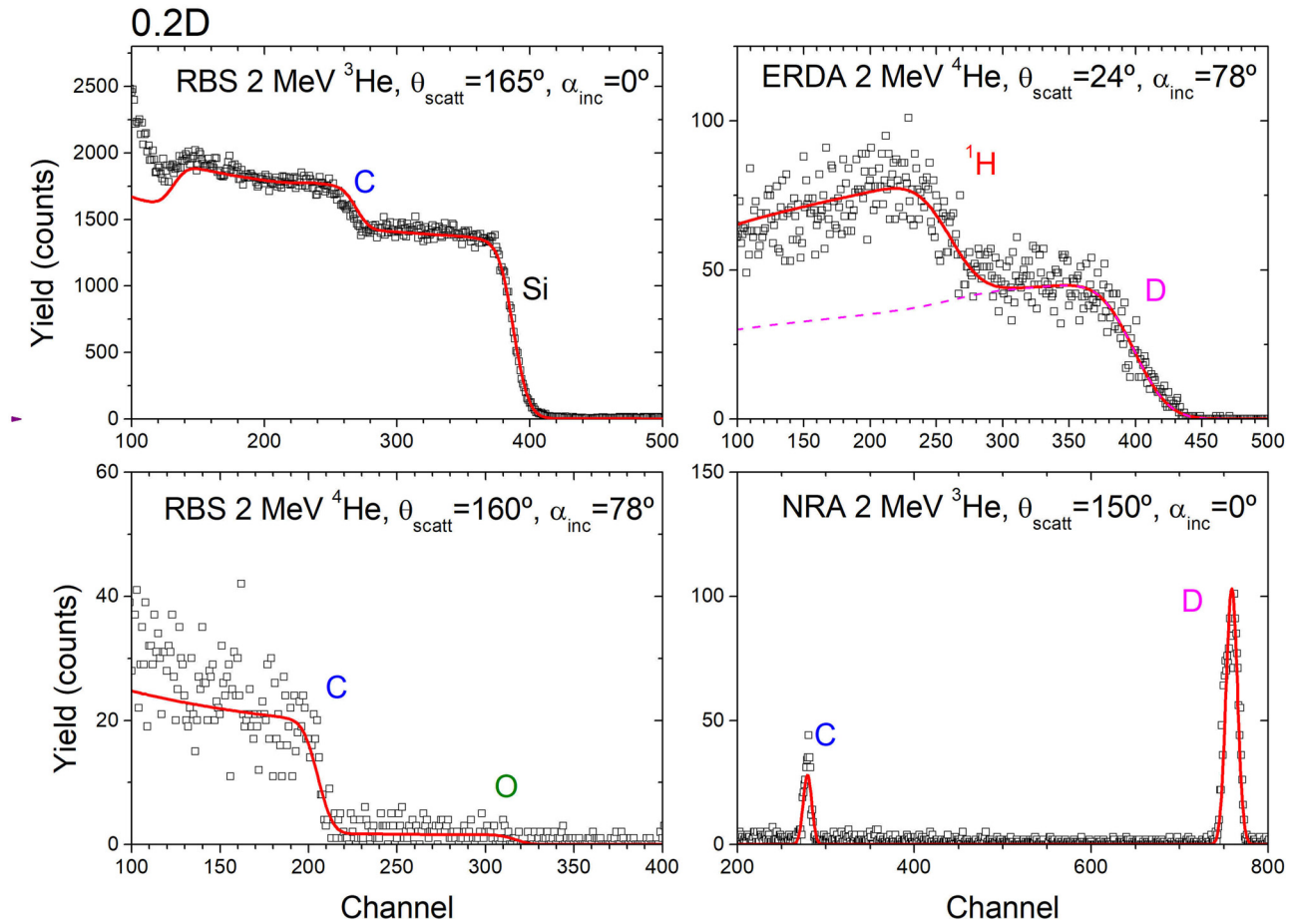


FIG. 2. (a) Representative SEM micrographs of the surface topography of the studied samples and (b) dependence of the deposition rate, discharge voltage, and discharge current on the D_2 fraction in the discharge gas (data for the reference sample without deuterium are placed at a D_2 content of 0.01%).



27 September 2023 15:45:06

FIG. 3. IBA data obtained for sample 0.2D. All data were analyzed simultaneously, with the same sample composition. The resulting fits are shown as red lines. The contributions of the identified elements are marked.

and theoretical (electron stopping powers and scattering cross sections) parameters. The uncertainties of about ± 3 at. % for the relative concentrations were calculated using the Bayesian inference method, implying increased relative uncertainty of the low-concentration elements. The uncertainty of the total areal densities N_t of the analyzed films, obtained using the same approach, is in the range of ± 0.7 –3%.

In all samples, no sign of varying composition with depth was observed within the uncertainties, i.e., the films seem to have no significant compositional variation in dependence of the film depth. The results are summarized in Table I and Fig. 4. Table I also includes the thickness d of the a-C films obtained by FIB-SEM, the total areal concentration N_t , as well as the averaged atomic (n) and mass (ρ) densities of the films calculated from the available data. By considering the uncertainties of N_t and d , the relative uncertainties of atomic and mass densities are in the range of 5%–6% and 5%–7%, respectively. The magnitude n was then used to determine absolute concentrations of detected elements from the

relative amounts obtained by fitting the IBA spectra [the latter are presented in Fig. 4(a)].

The total areal atomic density N_t of the thin films steadily increases with the number of incorporated impurities up to sample 1D and then abruptly drops for sample 10D. This result appears to be a surprise having in mind that the compositions of samples 1D and 10D are similar.

As expected, the amount of D in the films increases with its relative content in the discharge gas. The maximum possible amount of H atoms (and its isotopes) is about 65 at. %, which corresponds to the formation of aliphatic saturated hydrocarbons, e.g., paraffin. The latter can, at least partially, explain the saturation trend of the H/D concentration vs D_2 content in the discharge gas. Despite a careful procedure to minimize the outgassing from the system (full metal UHV system, 24h bakeout, target burn-in before opening the shutter for deposition), the reference sample contains almost 12 at. % of H and ~ 5 at. % of O. Absolute concentrations of incorporated H and O remain practically constant (apart from the

TABLE I. Relative atomic concentrations, thicknesses, and areal and atomic densities of the deposited carbon films determined by the IBA techniques and FIB-SEM.

| Sample | D (nm) | N_t (10^{16} cm^{-2}) | n (10^{23} cm^{-3}) | C (cm^{-3}) | D (cm^{-3}) | H (cm^{-3}) | O (cm^{-3}) | ρ (g/cm^3) |
|-----------|--------|-------------------------------------|-----------------------------------|------------------------|------------------------|------------------------|------------------------|----------------------------|
| Reference | 486 | 387 | 0.795 | 6.6×10^{22} | 0 | 0.9×10^{22} | 0.4×10^{22} | 1.44 |
| 0.2D | 482 | 574 | 1.19 | 9.3×10^{22} | 1.1×10^{22} | 1.2×10^{22} | 0.3×10^{22} | 1.99 |
| 0.5D | 564 | 720 | 1.28 | 8.6×10^{22} | 3.0×10^{22} | 0.8×10^{22} | 0.3×10^{22} | 1.91 |
| 1D | 587 | 1090 | 1.86 | 10.0×10^{22} | 7.4×10^{22} | 1.2×10^{22} | 0.3×10^{22} | 2.34 |
| 10D | 719 | 738 | 1.03 | 4.6×10^{22} | 5.2×10^{22} | 0.3×10^{22} | 0.2×10^{22} | 1.15 |

sample 10D) in all samples, as expected in the case of contamination originating from the residual gas in a baked system.

The IBA results concerning the in-depth uniformity of the sample composition are confirmed by the results of the dynamic SIMS measurements. As an example, we show in Fig. 4(b), the time dependence of the intensities of mass peaks attributed to H^+ , D^+ , C^+ , and Si^+ ions for the sample 0.5D during sputter depth-profiling. Except for the initial drop of signals of masses 1, 2, and 28 (most probably related to the surface contamination with H, D, and CO, respectively), the intensities are fairly constant. The same trend was observed for all other samples (except for the reference sample for which the signal attributed to D was on the noise level).

The average flux of an element incorporated into the film during the coating process can be calculated by multiplying its concentration (Table II) by the deposition rate in nm/h [Fig. 2(b)]. These quantities for C and D, presented in Fig. 5 for each of the analyzed samples, have the same trend: they increase with increasing deuterium content in the discharge gas up to 1.3% (sample 1D) and then decrease for sample 10D. While being generally expected for deuterium, such behavior is surprising for C atoms produced exclusively by the physical sputtering of pure graphite.

The increase of the discharge current, which takes place when adding deuterium to the discharge, is accompanied by a decrease in the discharge voltage [to maintain a constant power of 30 W, Fig. 2(b)]. The dark cathode space in magnetron discharges, which is typically a few millimeters wide, is considered to be free of collisions for an operation pressure of 2 Pa,²⁴ as generally confirmed with our estimations given in the supplementary material.⁵⁰ Therefore, to a good approximation, it can be considered that the impact energy of Ar^+ ions equals the discharge voltage. After calculating the energy-dependent sputtering yields of graphite by Ar projectiles using the empirical expression from,²⁵ the corresponding sputtering rates for each sample were estimated. If the discharge current exclusively corresponds to Ar^+ ions impinging the cathode, the sputtering rate and the overall flux of carbon atoms leaving the cathode due to the physical sputtering of pure graphite should slowly decrease with the content of deuterium in the discharge gas. Although the transport of sputtered particles from the target to the substrate will be affected by collisions with the gas particles, we do not expect that this effect will significantly depend on the amount of introduced D_2 . In other words, the deposition rate of C atoms should follow the same trend as the sputtering rate and, consequently, decrease by

27 September 2023 15:45:06

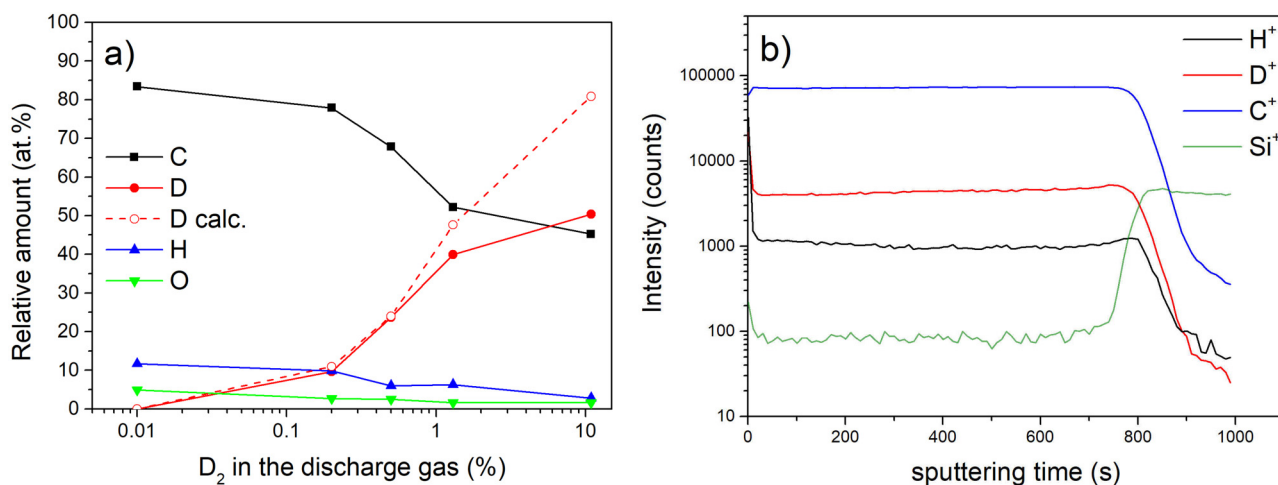


FIG. 4. (a) Composition analysis of the a-C coatings vs the D_2 content in the discharge gas performed by IBA, including the D content calculated in Sec. III C (data for the reference sample, without D_2 , are placed at 0.01%) and (b) time evolution of the SIMS signals corresponding to H^+ , D^+ , C^+ , and Si^+ during sputtering, taken from the sample 0.5D.

TABLE II. Calculation of the estimated relative content of deuterium in the films from the p_{D_2} drop when the discharge is ignited.

| Sample | $p_{D_2}^{off}$ (Pa) | $p_{D_2}^{on}$ (Pa) | D_2 fraction | $r^{net}(D^0)$ ($10^{16} s^{-1}$) | D content, calculated (at. %) |
|--------|----------------------|----------------------|----------------|--|-------------------------------------|
| 0.2D | 3.8×10^{-3} | 1.2×10^{-3} | 0.002 | 0.35 | 11.0 |
| 0.5D | 1.1×10^{-2} | 4.6×10^{-3} | 0.005 | 0.78 | 24.0 |
| 1D | 2.6×10^{-2} | 1.3×10^{-2} | 0.013 | 1.73 | 47.6 |
| 10D | 2.2×10^{-1} | 1.6×10^{-1} | 0.109 | 6.96 | 80.8 |

adding D_2 in the discharge gas. Therefore, another D-dependent mechanism plays a role in the deposition process, by enhancing the carbon sputtering rate.

It is worth noting that the increase of the discharge current with the D_2 partial pressure (and the consequent voltage decrease) is counterintuitive and requires further consideration. At constant power, adding D_2 in the discharge should reduce the discharge current since its ionization probability is significantly lower than that of Ar [e.g., in the case of 550 eV electrons, the electron impact ionization cross sections are $\sigma_{H_2} = 0.41 \times 10^{-20} m^2$ (Ref. 26) and $\sigma_{Ar} = 1.47 \times 10^{-20} m^2$ (Ref. 27)]. This behavior is, in fact, observed for the lowest partial pressures of deuterium [cf., Fig. 2(b)]. However, a further increase in the D_2 content contributes to the rapid increase of the discharge current. The most probable reason for this behavior is the poisoning of the target by hydrogen species. Formation of a hydrocarbon overlayer increases the ion-induced secondary electron yield compared to that of the initial graphite surface,^{28,29} and consequently, increases the discharge current. This suggests that target poisoning can be one of the steps leading to D incorporation in the films, which will be elaborated in Sec. IV.

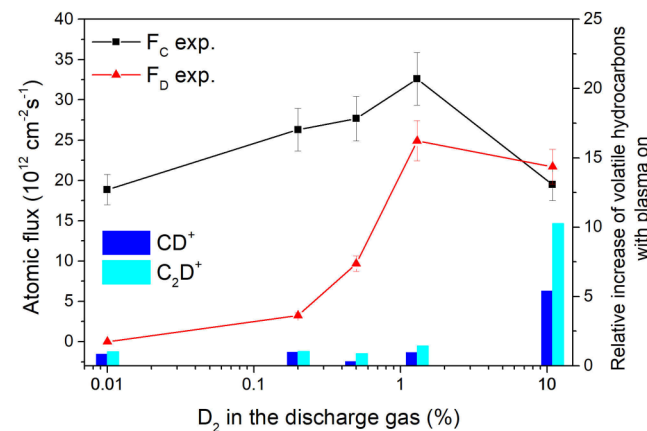


FIG. 5. Estimated fluxes of deposited carbon and deuterium atoms vs D_2 fraction in the discharge gas. Vertical scale on the right, the ratio of RGA signals corresponding to perdeuterated methane and acetylene after and prior ignition of the discharge. Data for the reference sample with no incorporated deuterium are placed at a D content of 0.01%.

C. Deuterium consumption during the film deposition

The gas composition monitoring during the deposition process by the differentially pumped residual gas analyzer revealed that the partial pressure of D_2 instantaneously drops when the discharge is ignited (see Table II). This drop reflects the consumption of D_2 that can be either partially incorporated into the growing film or converted into other volatile gas species. In general, D_2 could also chemically react in the gas phase with species sputtered from the graphitic target, such as atomic C. Although not identical, various scattering and excitation cross sections for D_2 are similar to those for H_2 within 30%.³⁰⁻³³ Since much more data are available for H_2 -based species than for those that originate from D_2 , we will use, when necessary, cross sections of the former for our estimations.

From the flux of C atoms deposited onto the substrate (Fig. 5), we estimate that their concentration in the discharge gas does not exceed $10^{10} cm^{-3}$. The D_2 consumption rate in a reaction, $D_2 + C + Ar \rightarrow CD_2 + Ar$, calculated using the equivalent rate constant for H_2 (Ref. 34) is, at least, five orders of magnitude smaller than the dissociation rate of D_2 by electron impact (evaluated using the corresponding rate constant calculated in Sec. IV and assuming the electron concentration of $10^{10} cm^{-3}$, the latter being typical for low power magnetron discharges²⁴). Knowing that D_2 cannot react with the chamber walls, the consumption of deuterium is almost exclusively mediated via the formation of D_2^+ and D^+ ions, and D^0 atoms. In the type of discharge considered in this study, the generation of D_2^+ and D^+ ions is much less probable than the dissociation of deuterium molecules into neutral atoms.³⁵ Therefore, we will consider that D_2 consumption is exclusively related to the generation of D^0 .

The net generation rate of deuterium atoms $r(D^0)$ can be calculated from the drop of the D_2 pressure when the discharge is ignited. The recombination of deuterium atoms into D_2 is already encompassed by the model (it will be shown later that even this process can be safely neglected). Therefore, deuterium atoms and ions will be most probably pumped out by interacting with solid surfaces coated with carbon, including the chamber walls, the substrate, and the target. When the discharge is turned off, we can write the following steady-state equation for the injected flow of D_2 gas $Q_{D_2}^{in}$ (Pa L/s) as

$$Q_{D_2}^{in} = p_{D_2}^{off} \cdot S_{D_2}, \quad (1)$$

with $p_{D_2}^{off}$ (Pa) being the partial pressure of deuterium when the discharge is off and S_{D_2} is the deuterium pumping speed, with a measured value of 2.7 l/s. When the discharge is turned on, part of the deuterium flow $Q_{D_2}^{con}$ is consumed by the system so that the steady-state equation becomes $Q_{D_2}^{in} - Q_{D_2}^{con} = p_{D_2}^{on} \cdot S_{D_2}$. By subtracting this equation from Eq. (1), one can calculate the consumed deuterium flow from the measured drop of the D_2 partial pressure. Moreover, if we divide $Q_{D_2}^{con}$ by kT (k being the Boltzmann constant and T the absolute gas temperature) and multiply by 2, the net consumption rate of D atoms can be calculated as

$$r^{net}(D^0) = \frac{2 \cdot S_{D_2} \cdot (p_{D_2}^{off} - p_{D_2}^{on})}{kT}. \quad (2)$$

As a rough approximation, one can consider that the relative content of deuterium c_D in the films is directly proportional to the

drop of the deuterium partial pressure when the discharge is turned on, which implies that $c_D = m \cdot r^{net}(D^0)$. The constant m was determined from the experimental results for sample 0.2D. The results of this estimation are presented in Table II.

The estimated relative concentration of deuterium, also presented in Fig. 4(a) (D calc.), practically coincides with the experimental values for the samples with a lower D content (up to the sample 0.5D). As for the last two samples, the calculation overestimates the D content. A relative deuterium content above 65% (calculated $c_D = 80.8\%$ for the sample 10D) is physically impossible, suggesting the existence of another process for deuterium consumption apart from the incorporation into the chamber walls, including the film on the substrates.

This process was revealed by performing residual gas analysis during the deposition and following the masses corresponding to fragmented ions of perdeuterated methane and acetylene. For perdeuterated methane, we followed mass 14 (CD^+) [since the signals for masses 18 (CD_3^+) and 20 (CD_4^+) are dominated by Ar^{++} (Ref. 36) and Ar^{++} (Ref. 37)]. For perdeuterated acetylene, we followed mass 26 (C_2D^+) [since 28 ($C_2D_2^+$) is dominated by CO^+]. These two volatile species are known to be produced in the processes of chemical sputtering.³⁶ In Fig. 5, we also present the ratio of the RGA intensity for the masses measured when the discharge “ON” and “OFF.” Up to sample 1D, the ratios remain at ~ 1 , showing that any production of volatile deuterated hydrocarbons during the coating process is not detectable by the RGA. However, for the sample 10D, as the discharge is ignited, the signal ratio related to CD_4 and C_2D_2 increases to 5 and 10, respectively, indicating that part of the consumed D_2 is converted into volatile hydrocarbon species, which is extracted by the pumping system. This agrees with the drop of the fluxes of deposited D and C observed for sample 10D (Fig. 5).

D. Secondary electron yield of the films

As already stated in Sec. II, the SEY of all samples was measured utilizing an appropriate technique in dependence of the film conductivity. The results of the SEY measurements are presented in Fig. 6. The SEY maximum steadily increases with the deuterium fraction in the discharge gas. This increase is particularly evident for the 10D sample although the overall relative amounts of D and H are not significantly higher than those in sample 1D. The primary electron energy at which the SEY reaches its maximum is about 230 eV for the first four samples and 280 eV for sample 10D. The significant increase of SEY_{max} accompanied with its shift toward higher primary electron energies is typical for a decreased conductivity and/or a wider energy gap of the material: it is less probable for internal secondary electrons to lose energy on their way out from the material, which increases their escape depth.

E. Optical properties and the band gap of the films

The optical transmittance and reflectance measured at normal incidence can be found in the supplementary material.⁵⁰ Preliminary measurements showed that the diffuse light reflection is negligible, as expected from the high flat surface morphology observed in SEM images [cf. Fig. 2(a)]. Oscillations of the signal for photon energies below 2 eV, particularly visible in the case of

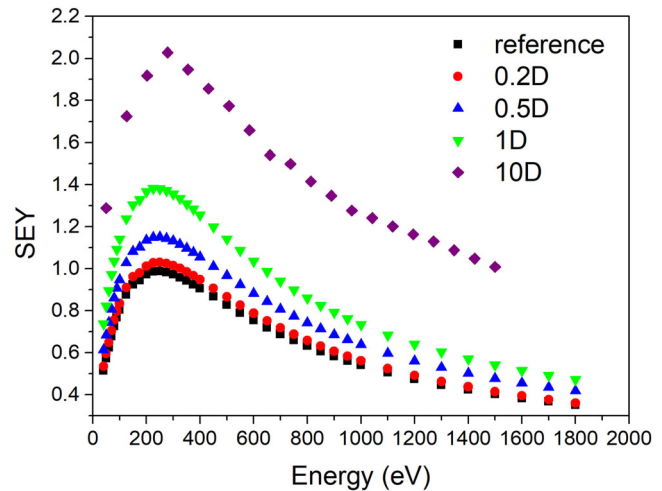


FIG. 6. Dependence of SEY of the carbon coatings on the electron primary energy.

reflectance, are evidence of interference effects. This motivated us to determine the absorption coefficient α from the calculated extinction coefficient, as described in Sec. III B.

Tauc plots obtained from the evaluated absorption coefficients of all five samples are presented in Fig. 7(a). Linear fits to the Tauc plots were performed in the energy ranges in which the plots are the steepest. Intersections of the lines obtained this way with the energy axis are usually interpreted as the energy gap of amorphous semiconductors,²¹ here denoted as Tauc gap E_T . The dependence of the maximum SEY (SEY_{max}) and the relative amount of D and H in the samples is presented in Fig. 7(b). Both the Tauc gap and SEY_{max} increase with the D/H content. Moreover, their dependencies are very similar, demonstrating a correlation between the two quantities that was already observed in Ref. 10.

It should be noted that the dependencies observed in Fig. 7(b) are quite linear up to sample 1D. In this range of H + D relative concentrations (11%–47%), both SEY_{max} and Tauc gap increase from 1 to 1.4 and from 0.1 to 1.2 eV, respectively. But then, both magnitudes steeply rise when this concentration changes only from 47% to 54%. Apparently, there is an abrupt change in the electronic structure when moving from sample 1D to 10D not directly related to the H and D content. This is also evident from the fact that only the sample 10D was nonconductive. The linear relation between the H content c_H and the Tauc gap E_T (eV) = $-0.9 + 0.09 \cdot c_H(\%)$ by Casiraghi *et al.*,³⁸ considered to be valid for $c_H > 20\%$, largely overestimates the measured energy gap [Fig. 7(b)]. A possible reason for this discrepancy could be non-uniformity of the deposited samples.

Indeed, a-C and hydrogenated/deuterated a-C (a-C:H/D) are frequently often nonuniform materials, consisting of different regions (e.g., graphitic, diamond-like, hydrocarbon-like, etc.).³⁹ Local energy gaps of diamond-like and various hydrocarbon phases are too large to justify the Tauc gap values around 2 eV or less. In these cases, the Tauc gap is related to the configuration of π states

27 September 2023 15:45:06

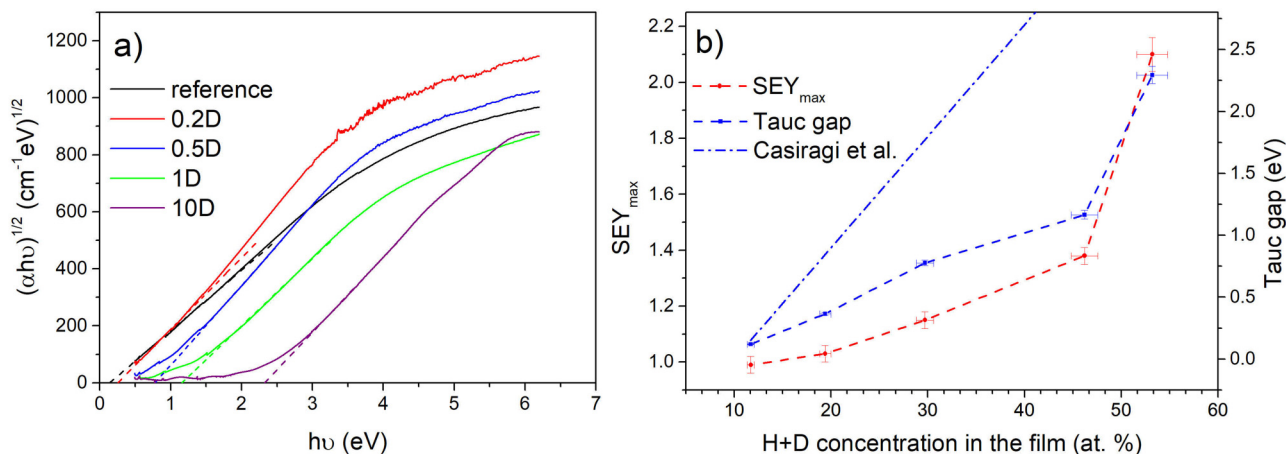


FIG. 7. (a) Tauc plots of the carbon coatings and (b) dependence of the Tauc gap E_T and SEY_{max} on the overall relative concentration of hydrogen and deuterium in the a-C coatings. The prediction of the model proposed by Casiraghi *et al.*³⁸ is also included.

on the sp^2 sites. Nevertheless, as a first estimation, we can propose dominant structures in different samples from the measured Tauc gaps and average mass densities (Table I) using the general guidelines proposed in Ref. 40 and having in mind that ρ of deuterated films is somewhat above those for equivalent a-C:H structures. The sample 10D, with its low mass density and E_T above 2 eV, appears to be a typical example of a polymer-like a-C:D. The reference and 0.2D samples (and to some extent, the sample 0.5D) with E_T well below 1 eV are most likely dominated by graphitic and graphite-like a-C:D. A further increase of deuterium content seems to be increasing the sp^3 content (mainly by saturating the double C=C bonds³⁹), which increases their density and contributes to the higher energy gap. The sample 1D, with its E_T of 1.38 eV, as well as high density and H+D content, appears to be closest to the diamond-like a-C:D.

IV. DISCUSSION

As already stated in Sec. B, the increase of the discharge current with the partial pressure of deuterium during the deposition can be explained by an increase in the ion-induced secondary electron yield of the graphite target, caused by the formation of hydrocarbons on the surface. The hydrocarbons are formed by the coirradiation by energetic ions and dissociated H/D atoms (as clearly explained in the frame of the Hopf model for chemical sputtering of hydrocarbon films^{37–42}). Incident ions break C—C bonds, which can then be saturated by H atoms impinging the surface. H poisoning transforms the conductive graphite surface into dielectric hydrocarbons, thus increasing the ion-induced secondary electron yield γ_e .²⁸ The latter causes the relative discharge current to increase within 5% for the first four samples and about 20% for the sample 10D (that has a polymeric nature). Knowing that γ_e of Ar^+ for various metals at 400–600 eV is around 10% and increases to 20%–35% due to the hydrocarbon

contamination,²⁹ it appears that the target surface becomes gradually contaminated by adding D_2 in the discharge gas.

Another consequence of target poisoning by hydrogen is the reduction of the surface binding energy (E_{SB}), causing an increase in the physical sputtering yield. As an example, if an accelerating ion impacts a perfect graphite (0001) surface, it must break three C—C bonds in order to eject a carbon atom. However, in the case of H (D) poisoning, each C—C bond that was broken by an impinging ion can be replaced by a C—H(D) bond, which reduces E_{SB} of C atoms. Indeed, this effect has been reported in the literature: good agreements between the measured sputtering yields of graphite and hydrogenated a-C and Monte Carlo simulations are obtained for E_{SB} equal to 4.5 and 2.8 eV, respectively.⁴¹ This reduction of E_{SB} doubles the physical sputtering yield of C. Considering a progressive increase of the target poisoning with deuterium as the fraction of D_2 gas in the discharge increases, this reduction of E_{SB} can explain the increase of the fluxes of C and D atoms to the substrate measured for samples 0.2D, 0.5D, and 1D (Fig. 5). At the same time, this seems contradictory with the drop observed for 10D.

The target poisoning is a result of its coirradiation by Ar^+ ions and H(D) atoms: the former break surface bonds, while the latter saturates them. The target will remain clean as long as the H(D): Ar^+ ratio is kept low. In another extreme, when the ratio is sufficiently high, chemical sputtering becomes dominant as described by the Hopf model: after breaking all bonds between a carbon atom and the solid by a few collisions with impinging Ar^+ and replacing them with C—H bonds, volatile hydrocarbons are formed, (CH_4 , C_2H_6 , etc.), that leave the target surface. These species will be evacuated by the pumping system instead of being deposited on the substrate. When they begin to appear in the discharge gas, a decrease in the deposition rate is expected, as observed in the case of sample 10D (sample 5).

Apart from the target poisoning resulting in the deposition of physically sputtered C_xD_y molecules, deuterium incorporation into

27 September 2023 15:45:06

the films by direct reaction of D neutrals with the physically sputtered C atoms deposited on the substrate cannot be excluded. However, if this was the dominant mechanism, we would not have observed an increase in the flux of C atoms at the substrate, with the D₂ partial pressure in the discharge as for samples 0.2D, 0.5D, and 1D (Fig. 5).

All the observations suggest that the incorporation of the D/H species in our films can be described by a reactive sputtering process in three steps: (1) dissociation of D₂/H₂ in the discharge; (2) target poisoning by coirradiation with ions (Ar⁺, H₂⁺/D₂⁺, and H⁺/D⁺) and the dissociated D/H atoms; and (3) sputtering of non-volatile C_xH(D)_y radicals which are deposited on the substrate together with the C atoms.

In practical applications, the aim is to reduce the pollution of the thin film by hydrogen resulting from outgassing. In any case, contamination is caused by a too-high H(D):Ar⁺ flux ratio. A possible way to reduce the contamination of the a-C films with D/H, for a given partial pressure of D₂/H₂ in the discharge gas, is to hinder their dissociation, which is the initial step in the process. This can be achieved by tuning the discharge parameters, which requires a deep understanding of the different electron impact-driven processes in the magnetron discharge. Assuming that the electrons in the discharge follow a Maxwell distribution, the rate constant for an arbitrary process in a plasma caused by electron impact can be calculated as

$$k = \int_0^{\infty} v_e \cdot f_M(E) \cdot \sigma(E) dE, \quad (3)$$

where v_e is electron velocity at kinetic energy E , f_M is the Maxwell distribution, and σ is the cross section of the process. The electron temperature in magnetron discharges is typically in the range from 2 to 20 eV.²⁴ Figure 8(a) includes the rate

constants calculated for the major processes that can be expected in an Ar + H₂ discharge as a function of the electron temperature in the range from 2 to 10 eV, calculated using the corresponding cross sections from Refs. 27 and 35. It appears that the most relevant events are the ionization of Ar atoms and the dissociation of H₂ (in a probability order, assuming a relatively low partial pressure of H₂ compared to Ar), while the probabilities for H₂⁺ and H⁺ formation is orders of magnitude lower. In addition, lower electron temperatures favor H₂ dissociation with respect to the other processes considered.

The average generation rate of different species can be calculated by multiplying the corresponding rate constant with the concentration of electrons, corresponding atoms (n_{Ar} for Ar ionization and n_{H2} for D₂ dissociation), and the plasma volume. Therefore, the generation rate ratio of Ar⁺ ions and neutral H atoms can be calculated as

$$\frac{r(Ar^+)}{r(H^0)} = \frac{k(Ar^+) \cdot n_{Ar}}{k(H^0) \cdot n_{H2}}. \quad (4)$$

An equivalent expression can be applied to the Ar + D₂ discharge gas.

The Ar⁺ ion formation rate can be estimated from the discharge current that should correspond to the number of Ar ions extracted from the plasma per second. Here, we neglect the recombination of Ar⁺ with electrons in the discharge since its calculated recombination rate (see the model in Ref. 43) is, in our case, about six orders of magnitude lower than the Ar⁺ generation rate. In addition, we assumed that 10% of the total discharge current corresponds to ion-induced secondary electrons. The net generation rate of D atoms $r^{net}(D^0)$, already estimated from the D₂ partial pressure drop (Table II), is a result of the balance between the generation rate of deuterium atoms by electron impact $r(D^0)$ and its Ar atom

27 September 2023 15:45:06

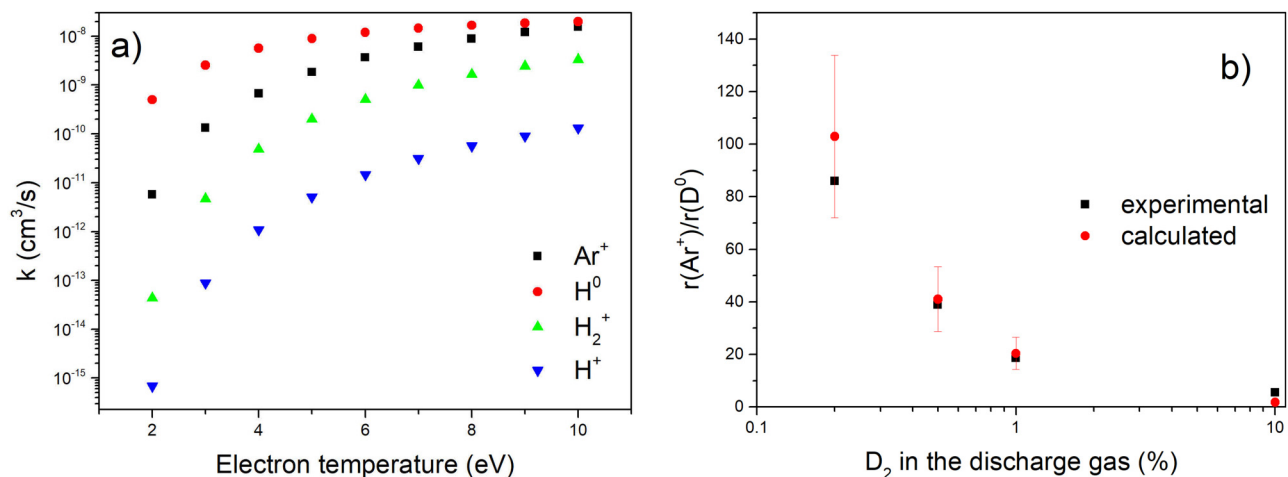


FIG. 8. (a) Formation rate constants of the most relevant electron impact-driven events in dependence of the electron temperature and (b) ratio of Ar⁺ and D⁰ generation rates estimated from the experiment and calculated for an assumed electron temperature of 5 eV. The error bars, estimated to be 30% of the calculated value, are due to the cross section uncertainty for D₂ dissociation.

supported recombination rate ($D + D + Ar \rightarrow D_2 + Ar$). Applying the equivalent rate constant for H,^{44,45} the concentration of D atoms from the p_{D_2} pressure drop and the known volumes of the plasma and the chamber, it appears that the recombination rate is about seven to eight orders of magnitude lower than the generation rate. Consequently, the experimental net generation rate of deuterium atoms $r^{net}(D^0)$ is practically identical to the actual generation rate $r(D^0)$.

The experimental values of $r(Ar^+)$ and $r(D^0)$ can be used to estimate the electron temperature using Eq. (4). The D_2 dissociation rate constant was calculated based on Eq. (3) by using the corresponding cross sections for H_2 (Ref. 35) due to the lack of reliable data for deuterium in a wide range of electron energies E_e . Calculations of the total dissociation cross sections in the E_e range from 9 to 12.5 eV show that the dissociation rate of D_2 is about 10%–30% higher than that of H_2 .³³ Measurements of the dissociation cross sections in the E_e range from 15 to 110 eV, based on the Balmer α (β) emission line, reveal that the cross section for H_2 is higher than that of D_2 by 10%–40% (15%–60%).³² Although using the dissociation cross sections for H_2 introduces some uncertainty, one should not expect deviations from the correct values of more than 30%. The results of the experimentally determined generation rate ratio of Ar^+ and D^0 as a function of the D_2 fraction in the discharge gas are shown in Fig. 8(b) together with the calculated values for an electron temperature of 5 eV.

The results presented in Fig. 8 suggest that the electron temperature in our discharge is ~ 5 eV, but also indicate that working at higher electron temperatures is expected to increase the ratio of the Ar^+ and D^0 generation rates and, thus, reduce the relative content of D atoms in the discharge. In addition, an increased concentration of Ar^+ ions (which implies a higher discharge current) will diminish the target poisoning by a reduction of H/D at the surface concentration due to enhanced physical sputtering at the target.

A few approaches could be considered to increase the electron temperature. Probably, the most straight-forward one is to increase the discharge power. The latter will also decrease the gas concentration in the vicinity of the target (due to the elevated gas temperature caused by thermal exchange with the target), which also increases the electron temperature²⁴ (though it may also induce higher thermal outgassing of H_2 from the vacuum system). Therefore, it is expected that a decrease in the operating pressure will also increase the electron temperature. The third approach could be changing the gas composition by adding a component having a higher ionization potential (e.g., Ne or He). In such a case, a higher energy of electrons would be required to sustain the discharge, although one should also consider that adding gases that are harder to be ionized will also reduce the rate constants for gas ionization.

The relevance of the incorporation of H/D atoms into the coatings by their transport through Ar gas from the discharge toward the substrate is a complex aspect, which is beyond the scope of this study. It depends on the fraction of H precursors in the discharge gas, discharge power, electron temperature (being directly related to the previous two issues), and particularly on the system geometry. In the case of extremely high H atomic fluxes at the substrate, one might expect a significant reduction

in the deposition rate due to the saturation of dangling bonds at the surface of a deposit.

The strong correlation between the values of SEY_{max} and the Tauc gap [cf. Fig. 7(b)], which was already observed in Ref. 10, offers an explanation for the SEY increase for a higher D content. Indeed, the opening of an energy gap increases the escape depth of internal secondary electrons, thus contributing to SEY growth. However, the cause of high nonlinear dependencies of SEY_{max} and the Tauc gap on the H/D content, in contrast to the expectations,³⁸ is still not clear. Discrepancy of the Tauc plot from the linear fit at low photon energies in Fig. 7(a) is usually attributed to Urbach tail states within the gap of amorphous semiconductors, caused by different defects in the material.⁴⁶ Alternatively, in the case of nonuniform systems representing a mixture of chemical phases, each phase could have its own energy gap and, consequently, a slope in the Tauc plot.⁴⁷

V. CONCLUSION

The influence of the incorporation of H into a-C coatings on their secondary electron emission properties is well established.^{48,49} In this work, this dependence was studied in further detail by deliberately introducing deuterium into the discharge gas of the magnetron sputtering system used to deposit the coatings. The latter resulted in the production of films that can be approximately considered as dominantly graphitic (reference, 0.2D), graphite-like a-C:D (0.5D), diamond-like a-C:D (1D), and polymer-like a-C:D (10D).

The experimental findings strongly indicate that the film contamination took place via poisoning of the graphite target by D, although its direct proof would require diagnostics of the magnetron discharge. In this scenario, the target poisoning occurs when D atoms, created in the discharge, saturate the surface dangling bonds that are simultaneously created by Ar^+ bombardment. Nonvolatile radicals (e.g., CD, CD_2 , and CD_3) are then physically sputtered from the poisoned target deposited onto the substrate. The concentration of D in the film increases with the D: Ar^+ flux ratio. In addition, at a sufficiently high partial pressure of D_2 , some fraction of carbon is etched in the form of volatile C_xD_y species (in a process known as chemical sputtering), which reduces the flux of the deposited species. At the same time, such samples have the highest D concentrations in the film. In general, the contamination mechanism strongly depends on the discharge parameters and particularly on the deposition system geometry.

If the concentration of D atoms in the gas phase near the substrate is sufficiently high, their direct impingement at the sample's surface becomes relevant. This condition is realistic when the substrate is in direct contact with the plasma (e.g., low discharge gas pressure, short target–substrate distance, or unbalanced magnetron configurations). However, the increase in the carbon deposition flux with the D_2 partial pressure observed for samples 0.2D, 0.5D, and 1D can only be explained in the frame of the target poisoning mechanism.

Sample contamination can be reduced by increasing the ratio of the Ar^+ and D^0 generation rates, which can be achieved by increasing the electron temperature in the discharge.

A strong correlation between the SEY_{max} and the Tauc gap¹⁰ was confirmed. For the first time, we established a correlation

between the change of SEY_{max} of an a-C coating with the actual amount of incorporated H/D. The SEY_{max} increases almost linearly from 12% up to ~47% of the sum of incorporated H and D in the film and then abruptly increases for further augmentation of the H+D content.

ACKNOWLEDGMENTS

This work was financed by the Portuguese Foundation for Science and Technology (FCT) in the frame of Project No. CERN/FIS-TEC/0039/2019. The support of FCT via Grant Nos. UIDB/00068/2020 and UIDP/00068/2020 is also gratefully acknowledged.

AUTHOR DECLARATIONS

Conflict of Interest

The authors have no conflicts to disclose.

Author Contributions

C. F. Adame: Conceptualization (supporting); Formal analysis (lead); Investigation (lead). **E. Alves:** Formal analysis (supporting); Methodology (equal); Supervision (equal); Validation (supporting). **N. P. Barradas:** Formal analysis (equal); Investigation (equal); Software (equal). **P. Costa Pinto:** Conceptualization (equal); Formal analysis (equal); Methodology (equal); Supervision (equal); Writing – original draft (lead). **Y. Delaup:** Formal analysis (equal); Investigation (equal); Validation (equal). **I. M. M. Ferreira:** Supervision (equal); Validation (equal). **H. Neupert:** Formal analysis (equal); Investigation (equal); Validation (equal). **M. Himmerlich:** Supervision (equal); Validation (equal); Writing – original draft (equal). **S. Pfeiffer:** Formal analysis (equal); Investigation (equal); Visualization (equal). **M. Rimoldi:** Formal analysis (equal); Investigation (equal); Validation (equal). **M. Taborelli:** Supervision (equal); Validation (equal); Writing – original draft (equal). **O. M. N. D. Teodoro:** Conceptualization (equal); Supervision (equal); Validation (equal); Writing – original draft (equal). **N. Bundaleski:** Conceptualization (lead); Methodology (equal); Supervision (lead); Writing – original draft (lead).

DATA AVAILABILITY

The data that support the findings of this study are available within the article.

REFERENCES

- ¹O. Gröbner, “Bunch induced multipactoring,” in *Proceedings of the 10th International Conference on High-Energy Accelerators, 11–17 July 1977*, Serpukhov, USSR (Protvino Institute for High Energy Physics, Serpukhov, Russia, 1977).
- ²R. Cimino, I. R. Collins, M. A. Furman, M. Pivi, F. Ruggiero, G. Rumolo, and F. Zimmermann, *Phys. Rev. Lett.* **93**, 014801 (2004).
- ³R. A. Kishek, Y. Y. Lau, L. K. Ang, A. Valfells, and R. M. Gilgenbach, *Phys. Plasmas* **5**, 2120 (1998).
- ⁴J. Puech *et al.*, “A multipactor threshold in waveguides theory and experiment,” in *Quasi-Optical Control of Intense Microwave Transmission*, edited by J. L. Hirshfield and M. I. Petelin (Springer, Dordrecht, 2005), pp. 305–323.
- ⁵J. Hillairet, M. Goniche, N. Fil, M. Belhaj, and J. Puech, “Multipactor in high power radio-frequency systems for nuclear fusion,” in *Proceedings of*

- MULCOPIIM 2017*, Noordwijk, The Netherlands (ESA/ESTEC, Noordwijk, the Netherlands, 2017).
- ⁶G. Skripka, G. Iadarola, L. Mether, and G. Rumolo, *Eur. Phys. J. Plus* **137**, 849 (2022).
- ⁷F. Zimmermann, “Electron cloud effects in accelerators,” in *CERN Yellow Reports Conference Proceedings 7*, edited by R. Cimino, G. Rumolo, and F. Zimmermann (CERN, Geneva, 2020), pp. 1–12.
- ⁸W. Fischer *et al.*, *Phys. Rev. Spec. Top.–Accel. Beams* **11**, 041002 (2008).
- ⁹C. Yin Vallgren *et al.*, *Phys. Rev. Spec. Top.–Accel. Beams* **14**, 071001 (2011).
- ¹⁰H. M. Fernández, M. Himmerlich, P. Costa Pinto, J. Coroa, D. Sousa, A. Baris, and M. Taborelli, *Appl. Surf. Sci.* **542**, 148552 (2021).
- ¹¹V. Baglin, H. Dupont, and T. Garcin, “Vacuum characterisation of a woven carbon fiber cryosorber in presence of H₂,” in *Proceedings of EPAC 2004*, Lucerne, Switzerland (EPS-AG, Mulhouse, France, 2004), pp. 1603–1605.
- ¹²P. Costa Pinto *et al.*, “In-situ amorphous carbon coating of the beam screens of LHC standalone magnets,” in *Oral communication at IPAC 20*, Caen, France (CERN EDMS, Geneva, 2020), p. 2639942.
- ¹³R. F. Egerton, *Electron-Energy Loss Spectroscopy in the Electron Microscope*, 3rd ed. (Springer, New York, 2011).
- ¹⁴N. P. Barradas and C. Jeynes, *Nucl. Instrum. Methods Phys. Res. B* **266**, 1875 (2008).
- ¹⁵J. F. Ziegler, J. P. Biersack, and M. D. Ziegler, *The Stopping and Range of Ions in Matter* (Ion Implantation, Chester, MD, 2008).
- ¹⁶A. F. Gurbich, *Nucl. Instrum. Methods Phys. Res. B* **371**, 27 (2016).
- ¹⁷N. P. Barradas and C. Pascual-Izarra, *Nucl. Instrum. Methods Phys. Res. B* **228**, 378 (2005).
- ¹⁸N. P. Barradas and M. Reis, *X-Ray Spectrom.* **35**, 232 (2006).
- ¹⁹N. P. Barradas, C. Jeynes, M. Jenkin, and P. K. Marriott, *Thin Solid Films* **343–344**, 31 (1999).
- ²⁰C. Pasqual-Izarra, M. A. Reis, and N. P. Barradas, *Nucl. Instrum. Methods Phys. Res. B* **249**, 780 (2006).
- ²¹J. Tauc and A. Menth, *J. Non-Cryst. Solids* **8–10**, 569 (1972).
- ²²P. P. Fiziev and D. R. Staicova, *Am. J. Comput. Math.* **2**, 95 (2012).
- ²³M. Pivi, F. K. King, R. E. Kirby, T. O. Raubenheimer, G. Stupakov, and F. Le Pimpec, *J. Appl. Phys.* **104**, 104904 (2008).
- ²⁴S. M. Rosnagel, “Magnetron plasma deposition processes,” in *Handbook of Plasma Processing Technology*, edited by S. M. Rosnagel, J. J. Cuomo, and W. D. Westwood (Noyes Publications, Park Ridge, 1990), pp. 160–182.
- ²⁵N. Matsunami, Y. Yamamura, Y. Itikawa, N. Itoh, Y. Kazumata, S. Miyagawa, K. Morita, R. Shimizu, and H. Tawara, *At. Data Nucl. Data Tables* **31**, 1 (1984).
- ²⁶W. Hwang, Y.-K. Kim, and M. E. Rudd, *J. Chem. Phys.* **104**, 2956 (1996).
- ²⁷H. C. Straub, P. Renault, B. G. Lindsay, K. A. Smith, and R. F. Stebbings, *Phys. Rev. A* **52**, 1115 (1995).
- ²⁸I. Figueiredo, N. Bundaleski, O. M. N. D. Teodoro, K. Jousten, and C. Illgen, *Vacuum* **184**, 109907 (2021).
- ²⁹A. V. Phelps and Z. Lj Petrović, *Plasma Sources Sci. Technol.* **8**, R21 (1999).
- ³⁰B. L. Carnahan and E. C. Zipf, *Phys. Rev. A* **16**, 991 (1977).
- ³¹C. S. Trevisan and J. Tennyson, *Plasma Phys. Controlled Fusion* **44**, 2217 (2002).
- ³²C. Karolis and E. Harting, *J. Phys. B: At. Mol. Phys.* **11**, 357 (1978).
- ³³J. S. Yoon, Y. W. Kim, D. C. Kwon, M. Y. Song, W. S. Chang, C. G. Kim, V. Kumar, and B. J. Lee, *Rep. Prog. Phys.* **73**, 116401 (2010).
- ³⁴D. Hussain and A. N. Young, *J. Chem. Soc. Faraday Trans. 2* **71**, 525 (1975).
- ³⁵J. S. Yoon, M. Y. Song, J. M. Han, S. H. Hwang, W. S. Chang, B. J. Lee, and Y. Itikawa, *J. Phys. Chem. Ref. Data* **37**, 913 (2008).
- ³⁶W. Jacob and J. Roth, “Chemical sputtering,” in *Sputtering by Particle Bombardment Experiments and Computer Calculations from Threshold to MeV Energies*, edited by R. Behrisch and W. Eckstein (Springer-Verlag, Berlin, 2007), pp. 329–400.
- ³⁷C. Hopf, A. von Keudell, and W. Jacob, *J. Appl. Phys.* **94**, 2373 (2003).
- ³⁸C. Casiraghi, A. C. Ferrari, and J. Robertson, *Phys. Rev. B* **72**, 085401 (2005).
- ³⁹A. C. Ferrari and J. Robertson, *Phys. Rev. B* **61**, 14095 (2000).
- ⁴⁰L. Zhang, X. Wei, and F. Wang, *Carbon* **94**, 202 (2015).

- ⁴¹W. Jacob, C. Hopf, and M. Schlüter, *Phys. Scr.* **T124**, 32 (2006).
- ⁴²M. Schlüter, C. Hopf, and W. Jacob, *New J. Phys.* **10**, 053037 (2008).
- ⁴³J. Stevefelt, J. Boulmer, and J.-F. Delpéch, *Phys. Rev. A* **12**, 1246 (1975).
- ⁴⁴N. Bundaleska, D. Tsyganov, R. Saavedra, E. Tatarova, F. M. Dias, and C. M. Ferreira, *Int. J. Hydrogen Energy* **38**, 9145 (2013).
- ⁴⁵C. L. Halstead and D. R. Jenkins, *Combust. Flame* **14**, 321 (1970).
- ⁴⁶J. A. Guerra, J. R. Angulo, S. Gomez, J. Llamaza, L. M. Montañez, A. Tejada, J. A. Töfflinger, A. Winnacker, and R. Weingärtner, *J. Phys. D: Appl. Phys.* **49**, 195102 (2016).
- ⁴⁷D. Roy, G. F. Samub, M. K. Hossain, C. Janáky, and K. Rajeshwar, *Catal. Today* **300**, 136 (2018).
- ⁴⁸P. Costa Pinto *et al.*, “Carbon coating of the SPS dipole chambers,” in *CERN Yellow Reports Conference Proceedings 2*, edited by R. Cimino, G. Rumolo, and F. Zimmerman (CERN, Geneva, 2013), pp. 141–148.
- ⁴⁹A. Santos, N. Bundaleski, B. J. Shaw, A. G. Silva, and O. M. N. D. Teodoro, *Vacuum* **98**, 37 (2013).
- ⁵⁰See the supplementary material online for derivation of the expressions for $R_{theor}(\lambda, n, \kappa, dI)$ and $T_{theor}(\lambda, n, \kappa, dI)$.